Separation of mainlobe and sidelobe contributions to B-mode ultrasound images based on the aperture spectrum

Rehman Ali,[a,b,*] **Trevor Mitcham**,[a] **Leandra Brickson**,[b] **Wentao Hu**,[c] **Marvin Doyley**,[c] **Deborah Rubens**,[a] **Zeljko Ignjatovic**,[c] **Nebojsa Duric**,[a,c] **and Jeremy Dahl**[b]

[a]University of Rochester Medical Center, Department of Imaging Sciences, Rochester, New York, United States

[b]Stanford University School of Medicine, Department of Radiology, Palo Alto, California, United States

[c]University of Rochester, Department of Electrical and Computer Engineering, Rochester, New York, United States

Abstract

Purpose: Isolating the mainlobe and sidelobe contribution to the ultrasound image can improve imaging contrast by removing off-axis clutter. Previous work achieves this separation of mainlobe and sidelobe contributions based on the covariance of received signals. However, the formation of a covariance matrix at each imaging point can be computationally burdensome and memory intensive for real-time applications. Our work demonstrates that the mainlobe and sidelobe contributions to the ultrasound image can be isolated based on the receive aperture spectrum, greatly reducing computational and memory requirements.

Approach: The separation of mainlobe and sidelobe contributions to the ultrasound image is shown in simulation, *in vitro*, and *in vivo* using the aperture spectrum method and multicovariate imaging of subresolution targets (MIST). Contrast, contrast-to-noise-ratio (CNR), and speckle signal-to-noise-ratio are used to compare the aperture spectrum approach with MIST and conventional delay-and-sum (DAS) beamforming.

Results: The aperture spectrum approach improves contrast by 1.9 to 6.4 dB beyond MIST and 8.9 to 13.5 dB beyond conventional DAS B-mode imaging. However, the aperture spectrum approach yields speckle texture similar to DAS. As a result, the aperture spectrum-based approach has less CNR than MIST but greater CNR than conventional DAS. The CPU implementation of the aperture spectrum-based approach is shown to reduce computation time by a factor of 9 and memory consumption by a factor of 128 for a 128-element transducer.

Conclusions: The mainlobe contribution to the ultrasound image can be isolated based on the receive aperture spectrum, which greatly reduces the computational cost and memory requirement of this approach as compared with MIST.

 [DOI: 10.1117/1.JMI.9.6.067001]

Keywords: aperture spectrum; coherence factor; spatial covariance; model-based image reconstruction.

Paper 22132GR received May 24, 2022; accepted for publication Oct. 12, 2022; published online Nov. 1, 2022.

1 Introduction

Medical ultrasound images are typically formed by delaying received signals according to the expected times-of-flight in the medium and coherently summing these delayed signals across the

*Address all correspondence to Rehman Ali, Rehman_Ali@URMC.Rochester.edu

2329-4302/2022/$28.00

receive aperture at each imaging point. This delay-and-sum (DAS) approach has long been the standard imaging approach on most ultrasound scanners to display the coherent backscatter intensity in the medium. Advancements in ultrasound imaging systems have enabled software beamforming, which allows for more sophisticated imaging approaches beyond standard DAS. Regardless of the transmit sequence used in acquisition, receive channel data are generally focused at every imaging point in the medium, so an array of receive signals across the aperture is given for each imaging point. Most software beamformers allow for advanced imaging techniques to be applied to the received ultrasound signal across the aperture at each imaging point to form images.

One group of these advanced imaging techniques is designed to measure the coherence of received signals across the aperture rather than the intensity of the backscattered ultrasound. Each of these coherence imaging techniques aims to remove the impact of backscatter intensity on the final image and relies on changes in signal coherence for imaging contrast. Coherence factor (CF),[1,2] initially described as an adaptive focusing criterion,[3] was defined as the ratio of the coherent sum over the incoherent sum of receive signals. Generalized coherence factor (GCF) expands upon CF using the spectrum across the receive aperture to measure the ratio of coherent to incoherent signal intensities.[4] Meanwhile, phase CF and sign CF[5] measure the alignment of the phase and sign, respectively, of the receive signals as a metric for coherence. Additionally, short-lag spatial coherence,[6,7] based on the van Cittert–Zernike (VCZ) theorem,[8] measures coherence as a function of element offset and integrates this coherence function up to a maximum element offset.

Whereas coherence imaging techniques ignore backscattered signal, other techniques aim to improve upon the quality of standard DAS B-mode images that generally retain changes in backscatter intensity. Spatial prediction filtering[9,10] employs an autoregressive model to the received signals prior to summation to remove noise and off-axis clutter in the final B-mode image. Furthermore, minimum variance,[11,12] delay-multiply-and-sum, and Wiener beamforming[13,14] have been used to suppress sidelobes and improve lateral resolution in B-mode images, whereas aperture domain model image reconstruction[15,16] applies a model and regularization scheme to detect and remove multipath scattering in the channel data prior to summation.

In addition to these prior works, recent work on multicovariate imaging of subresolution targets (MIST)[17–19] achieves the separation of mainlobe and sidelobe contributions to the ultrasound image by modeling and fitting the expected covariance across receive signals due to mainlobe and sidelobes, respectively. In MIST, the receive covariances due to mainlobe and sidelobe components are derived from the VCZ theorem.[8] However, a major challenge for real-time imaging with MIST is the number of computations performed and the storage required for each imaging point. For an N-element array, MIST requires N^2 computations and N^2 storage to form a covariance matrix for the receive signals at each imaging point.

The same decomposition approach used in MIST can be applied to the aperture spectrum of the received signals. In prior work,[2,4,20] the VCZ theorem was used to predict signal intensity in each frequency bin of the aperture spectrum in a diffuse-scattering medium with application to GCF. Although GCF uses the aperture spectrum to form coherence images, the same aperture spectrum can be used to separate mainlobe and sidelobe contributions to the ultrasound image without losing sensitivity to changes in backscatter intensity. Furthermore, achieving this separation based on the aperture spectrum would reduce computations to $O(N \log N)$ and storage to N at each imaging point. The goal of this paper is to demonstrate the separation of mainlobe and sidelobe contributions to the ultrasound image based on the aperture spectrum[21] and compare its performance with MIST.

2 Background and Theory

2.1 *Multicovariate Imaging of Subresolution Targets*

The MIST[17] technique aims to improve contrast in B-mode images by isolating and displaying only the mainlobe contributions to the image. This is achieved by formulating a model for the

covariance across receive elements for the mainlobe, sidelobes, and noise contributions to the image and fitting the observed covariance in the receive channel data to these components.

Figure 1 illustrates how the covariance components are constructed. The VCZ theorem[8] states that, in a diffuse scattering medium, there is a Fourier transform relationship between the autocorrelation of receive signals as a function of lag (i.e., element-offset) and the intensity distribution induced by the transmit aperture at the focus. Because the intensity distribution induced by a rectangular aperture is a sinc-squared profile [Fig. 1(a)], the autocorrelation across receive elements has a triangle shape that linearly decreases from 1 to 0 as the lag between the receive elements approaches the length of the transmit aperture [Fig. 1(b)]. The autocorrelation function can also be isolated for the mainlobe and sidelobe components of the source intensity distribution [Fig. 1(b)]. In Fig. 1(c), covariance matrices for the mainlobe (R_M) and sidelobe (R_S) contributions are symmetric oeplitz matrices constructed from their autocorrelation functions, and the covariance matrix for uncorrelated noise (R_N) is the identity matrix.[17]

We denote $\vec{s}(x,z)$ as a column vector of analytic signals across the receive aperture at some imaging point (x,z). MIST estimates the mainlobe ($\alpha_M(x,z)$), sidelobe ($\alpha_S(x,z)$), and noise ($\alpha_N(x,z)$) contributions at each imaging point using the following non-negative least squares optimization problem:

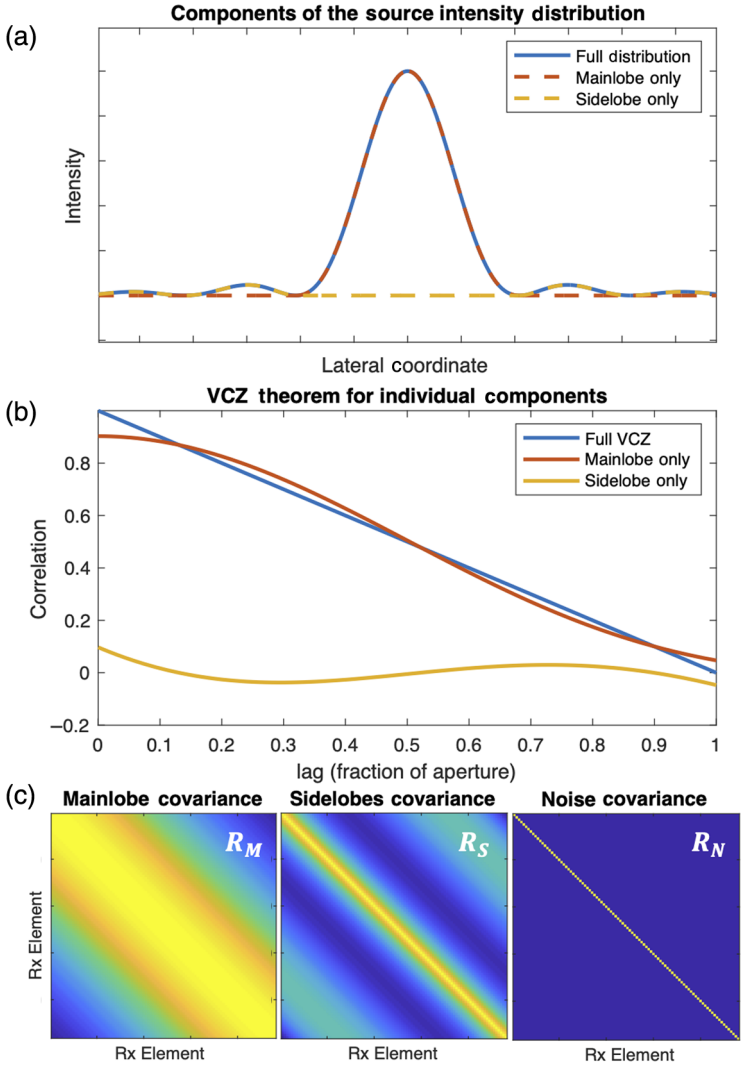

Fig. 1 Deriving the covariance components of MIST: (a) far-field lateral profile for mainlobe and sidelobe components. (b) Correlation versus lag based on the VCZ theorem for the full intensity profile, mainlobe only, and sidelobes only. (c) Covariance matrices for the mainlobe, sidelobes, and noise components, respectively.

$$\begin{bmatrix} \alpha_M^2 \\ \alpha_S^2 \\ \alpha_N^2 \end{bmatrix} = \underset{\substack{\alpha_M^2 \geq 0 \\ \alpha_S^2 \geq 0 \\ \alpha_N^2 \geq 0}}{\arg\min} \|\vec{s}\vec{s}^H - \alpha_M^2 R_M - \alpha_S^2 R_S - \alpha_N^2 R_N\|_2^2. \tag{1}$$

This implementation of MIST is equivalent to the three-component model and 0λ kernel used in the prior work.[17] A final image of $\alpha_M(x, z)$ yields a B-mode image with contributions from sidelobes and noise removed.

2.2 *Separation Based on the Aperture Spectrum*

Although MIST can isolate the mainlobe contribution to the ultrasound image, N^2 computations and N^2 storage are needed to form and store the covariance matrix $\vec{s}\vec{s}^H$ of the received signals across the aperture at each imaging point. The goal of this section is to present an alternative approach that reduces the computational and storage requirements to $O(N \log N)$ and N, respectively, by extending the underlying model used in MIST.

For an N-element array, the same vector $\vec{s}(x, z)$ as used in MIST has elements

$$\vec{s} = \begin{bmatrix} s[0] \\ s[1] \\ \vdots \\ s[N-1] \end{bmatrix}. \tag{2}$$

The discrete Fourier transform (DFT) of signals $s[i]$ across the array is

$$p[k] = \sum_{i=0}^{N-1} s[i] e^{-j2\pi ki/N}, \tag{3}$$

$$\vec{p} = \begin{bmatrix} p[-N/2] \\ \vdots \\ p[0] \\ \vdots \\ p[N/2-1] \end{bmatrix}, \tag{4}$$

$$\vec{p}(x, z) = \mathcal{F}\vec{s}(x, z), \tag{5}$$

where $\mathcal{F}$ is the DFT matrix.

Denote $\vec{a}_{\text{obs},L}(x, z)$ as the aperture spectrum across receivers:

$$\vec{a}_{\text{obs},L} = \begin{bmatrix} |p[-L]|^2 \\ |p[-L+1]|^2 \\ \vdots \\ |p[0]|^2 \\ \vdots \\ |p[L-1]|^2 \\ |p[L]|^2 \end{bmatrix}. \tag{6}$$

If the covariance matrix of received channel data $\vec{s}$ is given by R, the covariance of the frequency bins in $\vec{p}$ is given by $\mathcal{F}R\mathcal{F}^H$. As a result, the expected value of the aperture spectrum

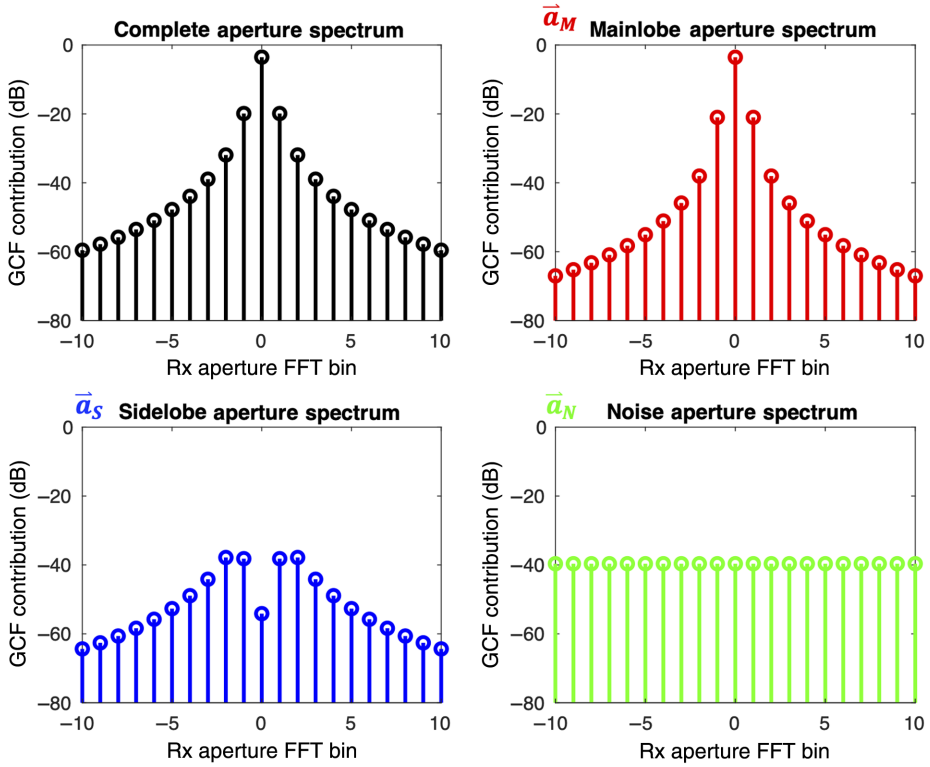

Fig. 2 Aperture spectrum based on the VCZ theorem for the full PSF, mainlobe component, sidelobe component, and noise for $L = 10$ on a 96-element transducer array. In contrast with Figure 2 from the proceedings paper,[21] this plot shows the aperture spectrum on a fixed logarithmic decibel (dB) scale rather than on a variable linear scale for visualization purposes. However, the decomposition described in Eq. (7) occurs on a linear scale.

$\vec{a}_{\text{obs},L}$ is given by the diagonal entries of $\mathcal{F}R\mathcal{F}^H$. The expected mainlobe, sidelobe, and noise contributions to the aperture spectrum ($\vec{a}_{M,L}(x,z)$, $\vec{a}_{S,L}(x,z)$, and $\vec{a}_{N,L}(x,z)$) are the diagonal entries of $\mathcal{F}R_M\mathcal{F}^H$, $\mathcal{F}R_S\mathcal{F}^H$, and $\mathcal{F}R_N\mathcal{F}^H$, respectively. Figure 2 shows the aperture spectra for the mainlobe, sidelobes, and noise for $L = 10$ on a 96-element transducer array.

The following non-negative least squares optimization problem is solved to separate the contributions of the mainlobe ($\beta_M(x,z)$), sidelobes ($\beta_S(x,z)$), and noise ($\beta_N(x,z)$) to the ultrasound image:

$$\begin{bmatrix} \beta_M^2 \\ \beta_S^2 \\ \beta_N^2 \end{bmatrix} = \underset{\substack{\beta_M^2 \geq 0 \\ \beta_S^2 \geq 0 \\ \beta_N^2 \geq 0}}{\arg\min} \|\vec{a}_{\text{obs},L} - \beta_M^2 \vec{a}_{M,L} - \beta_S^2 \vec{a}_{S,L} - \beta_N^2 \vec{a}_{N,L}\|_2^2. \tag{7}$$

A final image of $\beta_M(x,z)$ isolates the mainlobe contributions to the B-mode image with contributions from sidelobes and noise removed. By modeling the aperture spectrum instead of the covariance structure of the received ultrasound signals, the complexity and storage requirements for isolating the mainlobe contribution to the ultrasound image are greatly reduced. This image reconstruction is parameterized by L, the number of frequency bins to the left and right of the zero-frequency bin used in the non-negative least-squares problem [Eq. (7)]. As portrayed by Fig. 2, the low-frequency bins in the aperture spectrum contain the most important information relevant to the separation of mainlobe and sidelobe contributions to the image. However, if L is made too small, the imaging technique may not be sufficiently robust to noise encountered in most real channel data. This decomposition relies on the correlation between frequency bins in the aperture spectrum for the mainlobe, sidelobes, and noise, so a sufficiently large L is required

to adequately estimate their individual contributions to the image. If L is not specified, the full aperture spectrum ($L = N/2$) is used to favor robustness.

3 Experimental Methods

3.1 *Imaging Metrics*

Contrast, contrast-to-noise-ratio (CNR), and speckle signal-to-noise-ratio (SNR) were used to evaluate each imaging technique used in this work. They are defined as

$$\text{contrast} = 20\log_{10}\left(\frac{\mu_T}{\mu_B}\right), \tag{8}$$

$$\text{CNR} = \frac{|\mu_T - \mu_B|}{\sqrt{\sigma_T^2 + \sigma_B^2}}, \tag{9}$$

$$\text{speckle SNR} = \frac{\mu_B}{\sigma_B}, \tag{10}$$

where μ and σ^2 are the mean and variance of image values in the target (T) and background (B) regions of interest (ROIs), respectively.[17] In simulations, these ROIs were centered around a circular lesion target in which the target region was defined in a circular region with a radius that is 0.5 mm less than radius of the imaging target and the background was defined as being outside a circular region with a radius that is 0.5 mm more than the radius of that imaging target. For experimentally acquired data, these ROIs were determined by finding the largest circular regions corresponding to target and background at roughly the same imaging depth.

3.2 *Field II Simulations*

Radio-frequency channel data for a multistatic synthetic aperture transmit sequence described in Table 1 were simulated in field II[22,23] for a medium with a point target at 30-mm depth and media filled with random diffuse point scatterers with reflectivities that were modified to simulate anechoic, hypoechoic, and hyperechoic lesions.

The anechoic lesions were centered at 30-mm depth with radii of 2.0, 2.5, 3.0, 3.5, and 4.0 mm. Contrast and CNR were measured between an anechoic region contained inside a circle with a radius that is 0.5 mm smaller than the radius of the anechoic lesion and the speckle region outside of a circle with a radius that is 0.5 mm larger than the radius of the lesion. The speckle SNR of the background speckle was also quantified. The hypoechoic and hyperechoic lesions with ± 6, ± 12, ± 18, and ± 24 dB contrast were centered at 30-mm depth with a radius of 3.0 mm. The purpose of these hypoechoic and hyperechoic lesion simulations was to demonstrate the preservation of the intrinsic contrast of the imaging target.

For each set of simulations, the performance of DAS beamforming, DAS beamforming with CF weighting,[13,24] MIST, and the proposed aperture spectrum approach are compared for a variety of L values. Additionally, the contrast, CNR, and speckle SNR were measured as a function of the SNR of the received channel data. The simulated SNR of the channel data ranged from -40 to $+40$ dB by modulating the addition of white noise to the received signals.

Table 1 Siemens 5V1 array geometry and transmit pulse.

Parameter	Value	Units
Array geometry	(Phased) linear	—
Number of elements	96	Elements
Element pitch	0.215	mm
Center frequency	3.5	MHz

Table 2 P4-1 array geometry and transmit pulse.

Parameter	Value	Units
Array geometry	(Phased) linear	—
Number of elements	96	Elements
Element pitch	0.295	mm
Center frequency	2.5	MHz

3.3 *Additional In Vitro Evaluation of Lesion Contrast Using a Phased Array*

Radio-frequency channel data for a multistatic synthetic aperture acquisition described in Table 2 was acquired on a P4-1 phased-array transducer (ATL Technology, Springville, Utah) using a Verasonics Vantage 256 scanner (Verasonics, Kirkland, Washington). The multistatic synthetic aperture consists of receive channel data from each single-element transmission and was acquired using a Hadamard sequence from a modified Vantage script. An ATS Model 539 phantom (CIRS, Norfolk, Virginia) was imaged using this transmit sequence to evaluate the lesion contrast, CNR, and speckle SNR in anechoic, hypoechoic, and hyperechoic lesions to characterize each imaging technique.

3.4 *Phantom and Cardiac Imaging Examples*

A Siemens research scanner (Siemens Healthineers, Mountain View, California) was used to acquire focus transmit channel data from a 5V1 phased array transducer from point target phantoms and a healthy human volunteer. An apical four-chamber view and a parasternal long-axis view of the heart were acquired. Written informed consent was obtained under an institutional review board (IRB)-approved protocol. The transmit sequence is described in Table 3. The half-circle apodization describes the shape of the weighting given to each transducer element in the transmit aperture and is given by $w(x_n) = \sqrt{(D/2)^2 - x_n^2}$, where D is the length of the transmit aperture and x_n is the lateral position of the n'th transducer element ($x_n = 0$ is defined as the center of the probe). We compare DAS beamforming, MIST, and the proposed aperture spectrum approach using the entire aperture spectrum. We also demonstrate the impact of virtual source synthetic aperture (based on an architecture-specific implementation for the Siemens research scanner) on the aperture spectrum approach.[19] Additional field II simulations matching the transmit sequence in Table 3 and acquisition setup of the Siemens research scanner were also passed through a software model of the Siemens architecture to test the aperture spectrum method.

3.5 *Thyroid and Carotid Imaging Examples*

Two different transmit sequences on linear arrays from two different ultrasound systems were used to acquire radiofrequency channel data from the thyroid and carotid of healthy human volunteers under IRB-approved protocols. A different volunteer was imaged with each system, and

Table 3 Vector-scan transmit sequence on Siemens 5V1.

Parameter	Value	Units
Focal depth	120	mm
Transmit angle (θ) range	[−42, 42]	deg
$\Delta \sin \theta$	0.01654	—
Beam origin (x_o) locations	1.02125 tan θ	mm
Transmit apodization	Half-circle	—

Table 4 Walking-aperture focused-transmit sequence on Siemens 10L4.

Parameter	Value	Units
Array geometry	Linear	—
Number of elements	192	Elements
Element pitch	0.201	mm
Focal depth	20	mm
Transmit angle	0	deg
Beam origin range	[−19.3, 19.3]	mm
Beam origin step	0.19442	mm
Number of transmit beams	200	—
Aperture width	9.779	mm
Transmit apodization	Half-circle	—

written informed consent was obtained in each case. Table 4 summarizes the walking-aperture focused-transmit sequence implemented on a Siemens research scanner with an L10-4 probe. The walking aperture refers to the fact that each transmit beam does not use the entire array to produce the beam. Instead, a subsection of the array defined by the aperture width and beam origin is used to create the transmit beam. The beam origin is stepped (or walked) across the array to produce each image line. Additionally, a multistatic synthetic aperture dataset consisting of received channel data from single-element transmissions (7.8 MHz) was acquired from the center 128 elements on an L12-3v (0.2-mm pitch) transducer using a Verasonics Vantage 256 scanner.

Each imaging setup uses a similar frequency band and element spacing to image the thyroid and carotid. However, the main difference between these imaging setups comes from their respective transmit sequences. The single-element transmissions used on the L12-3v yields much lower channel data SNR than the focused transmissions used on the Siemens L10-4 probe. In each case, contrast, CNR, and speckle SNR were measured between the thyroid and carotid.

3.6 *Abdominal Imaging Examples*

Table 5 summarizes the walking-aperture focused-transmit sequence implemented on a Siemens research scanner with a 5C1 probe. Radiofrequency channel data were acquired *in vivo* from the

Table 5 Walking-aperture focused-transmit sequence on Siemens 5C1.

Parameter	Value	Units
Array geometry	Curvilinear	—
Probe radius	46.03	mm
Number of elements	180	Elements
Element pitch	0.3212	mm
Transmit focal depth	97	mm
Beam angles	[−36.103, 36.103]	deg
Number of transmit beams	121	—
Spacing between beams	0.6017	deg

abdomen of a healthy human volunteer under an IRB-approved protocol, and written informed consent was obtained. Contrast, CNR, and speckle SNR were measured between the gallbladder and liver.

4 Results

4.1 *Separation of Mainlobes and Sidelobes in Point Targets*

Figure 3 shows the separation of mainlobe and sidelobes in a field II-simulated point target using MIST and the proposed aperture spectrum approach using $L = 3,4,5,6,7,8$ and the full aperture

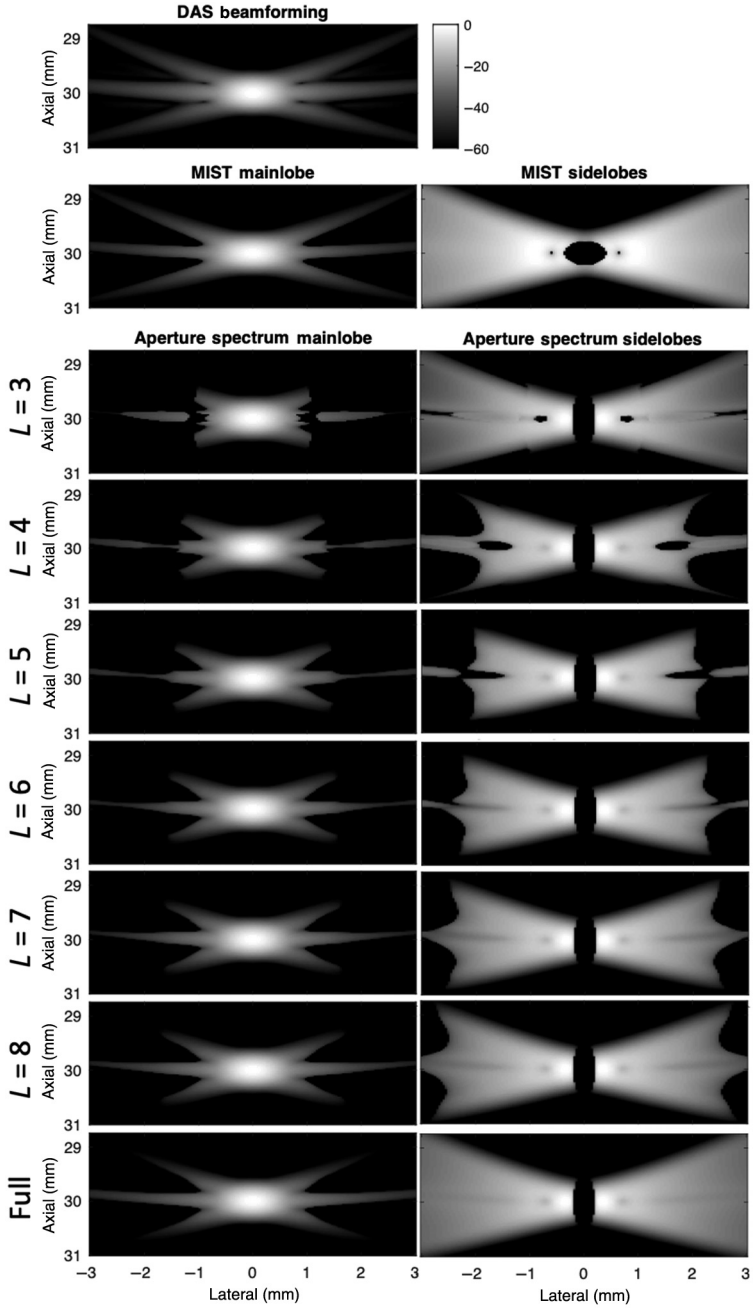

Fig. 3 Separation of mainlobes and sidelobes in a point target using MIST and the proposed aperture spectrum approach.

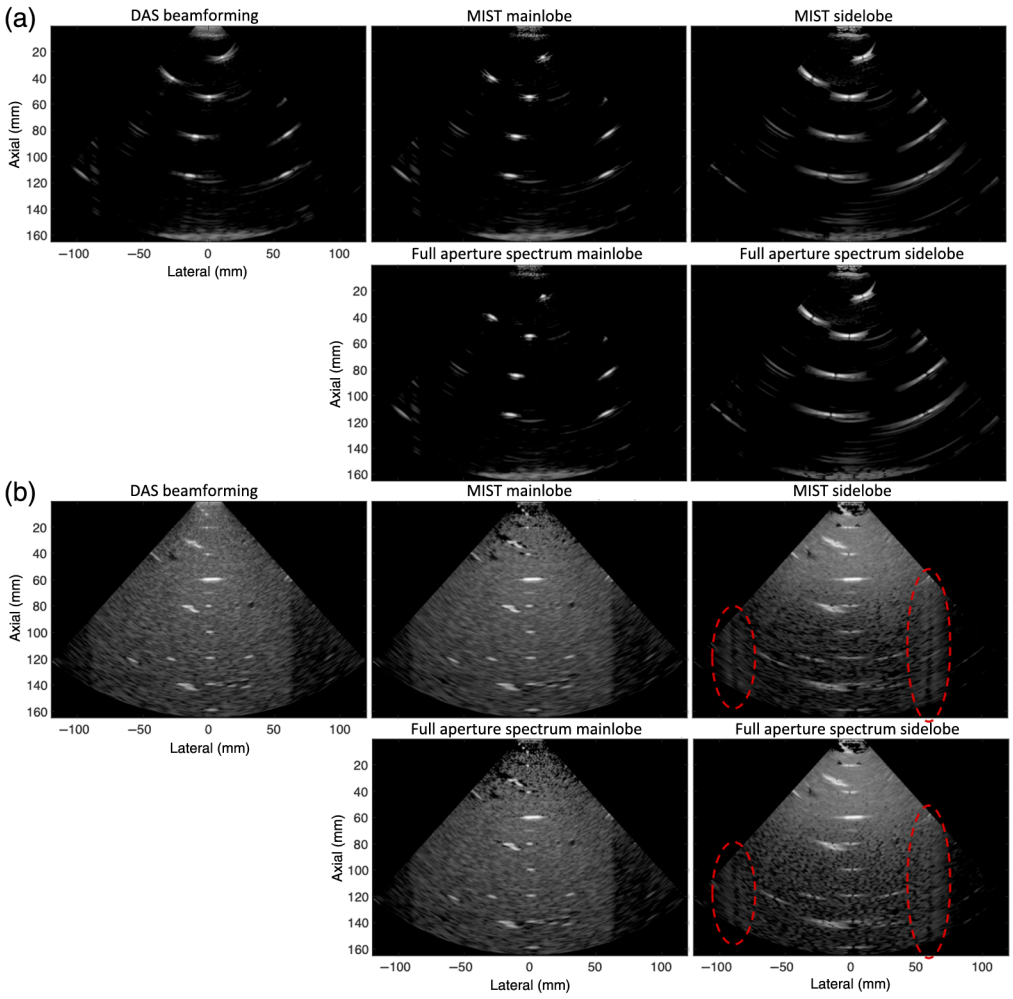

Fig. 4 Separation of mainlobes and sidelobes in point targets using MIST and the proposed aperture spectrum approach in phantom experiments with vector scan sequence on Siemens 5V1 array (Table 3). (a) Point targets in an anechoic background and (b) point targets in a diffuse scattering background. The red circles highlight the sidelobes induced by the sudden change in backscatter intensity at the edges of the phantom. Each image is shown at the 60-dB dynamic range.

spectrum. In each case, the reconstructed mainlobe image from the aperture spectrum approach suppresses the tails of the point spread function (PSF) more strongly than with MIST. As L decreases in the aperture spectrum approach, the tails of the PSF are more strongly suppressed in the mainlobe image.

Figure 4 shows point targets in phantoms captured using the Siemens 5V1. The same decomposition of mainlobe and sidelobes is shown using MIST and the aperture spectrum approach using the entire aperture spectrum. Figure 4(a) shows a clear separation between the mainlobe and sidelobes for each point target with both techniques. The aperture spectrum approach shows visibly tighter point targets in the mainlobe image as compared with MIST. Figure 4(b) shows point targets in a diffuse-scattering background. Because both MIST and the aperture spectrum methods are based on the VCZ theorem applied to diffuse-scattering media, the purpose of this phantom experiment is to assess the separation of mainlobe and sidelobes in point targets when placed in a diffuse-scattering background medium. Although both MIST and the aperture spectrum approaches continue to separate the mainlobe and sidelobes for each point target, the quality of this separation improves at imaging depths close to the transmit focal depth of 120 mm. The dashed red circles in Fig. 4(b) highlight the sidelobes induced by the sudden change in backscatter intensity at the edges of the phantom.

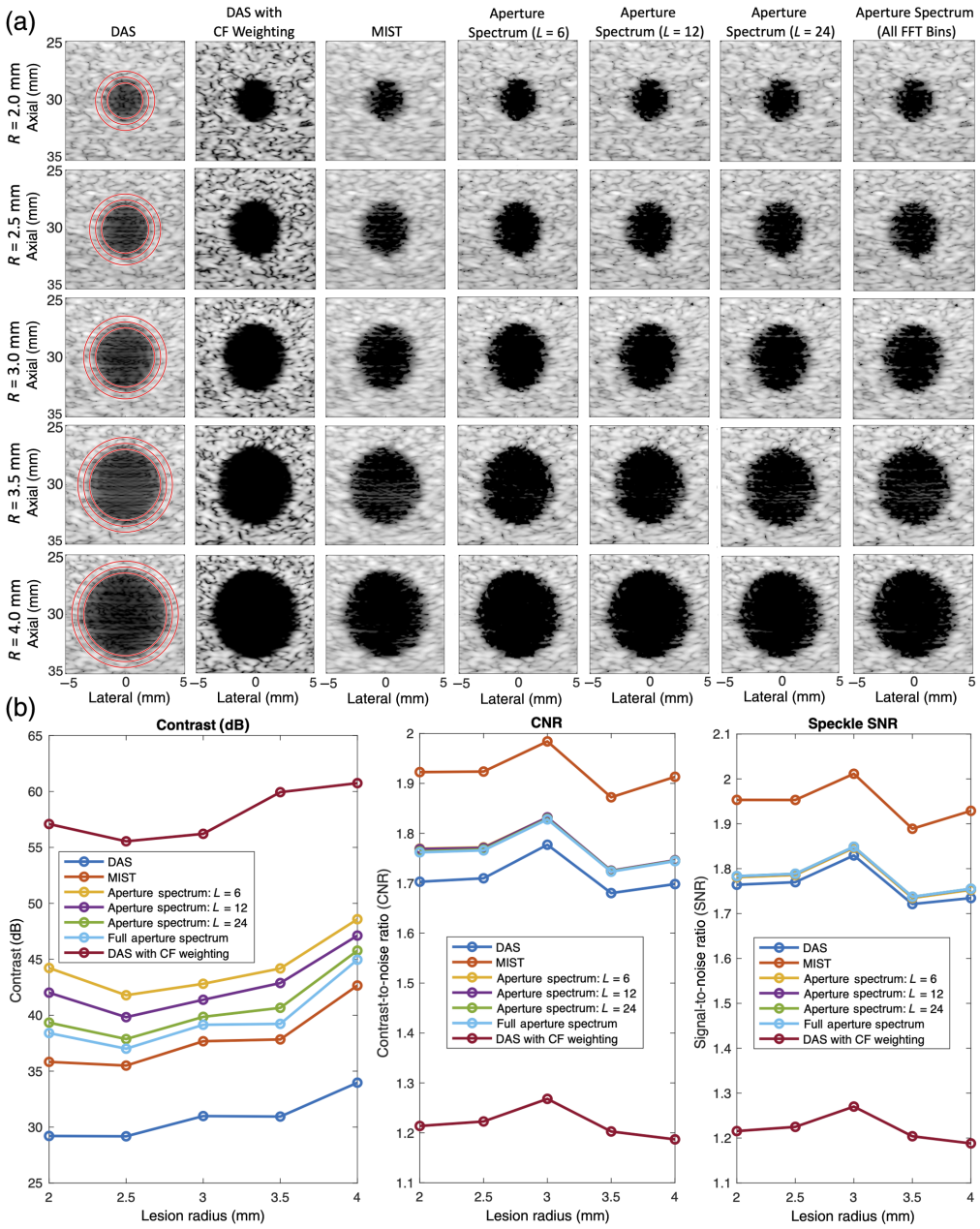

Fig. 5 Comparison of DAS beamforming, MIST, and the proposed aperture spectrum methods in simulated anechoic lesions. (a) The lesion area inside the innermost red-circle and speckle region outside the outermost red circle are the target (T) and background (B) ROIs, respectively, for Eqs. (8)–(10). All images are shown at the 60-dB dynamic range. (b) Measurements of lesion contrast, lesion CNR, and speckle SNR for DAS beamforming, DAS with CF weighting, MIST, and the proposed aperture spectrum methods ($L = 6,12,24$, and the full aperture spectrum).

4.2 *Performance in Anechoic Lesions*

Figure 5(a) shows DAS, DAS with CF weighting, MIST mainlobe, and aperture spectrum mainlobe ($L = 6,12,24$, and the full aperture spectrum) images for simulated anechoic cysts having radii of 2.0, 2.5, 3.0, 3.5, and 4.0 mm. Both MIST and the aperture spectrum approaches reduce sidelobe clutter within the anechoic lesion. The aperture spectrum approach has visibly less sidelobe clutter within the lesion, especially at lower values of L. Figure 5(b) plots the lesion contrast, lesion CNR, and speckle SNR for each imaging technique as a function of the lesion radius. The lesion contrast and CNR are computed between the lesion area inside the innermost

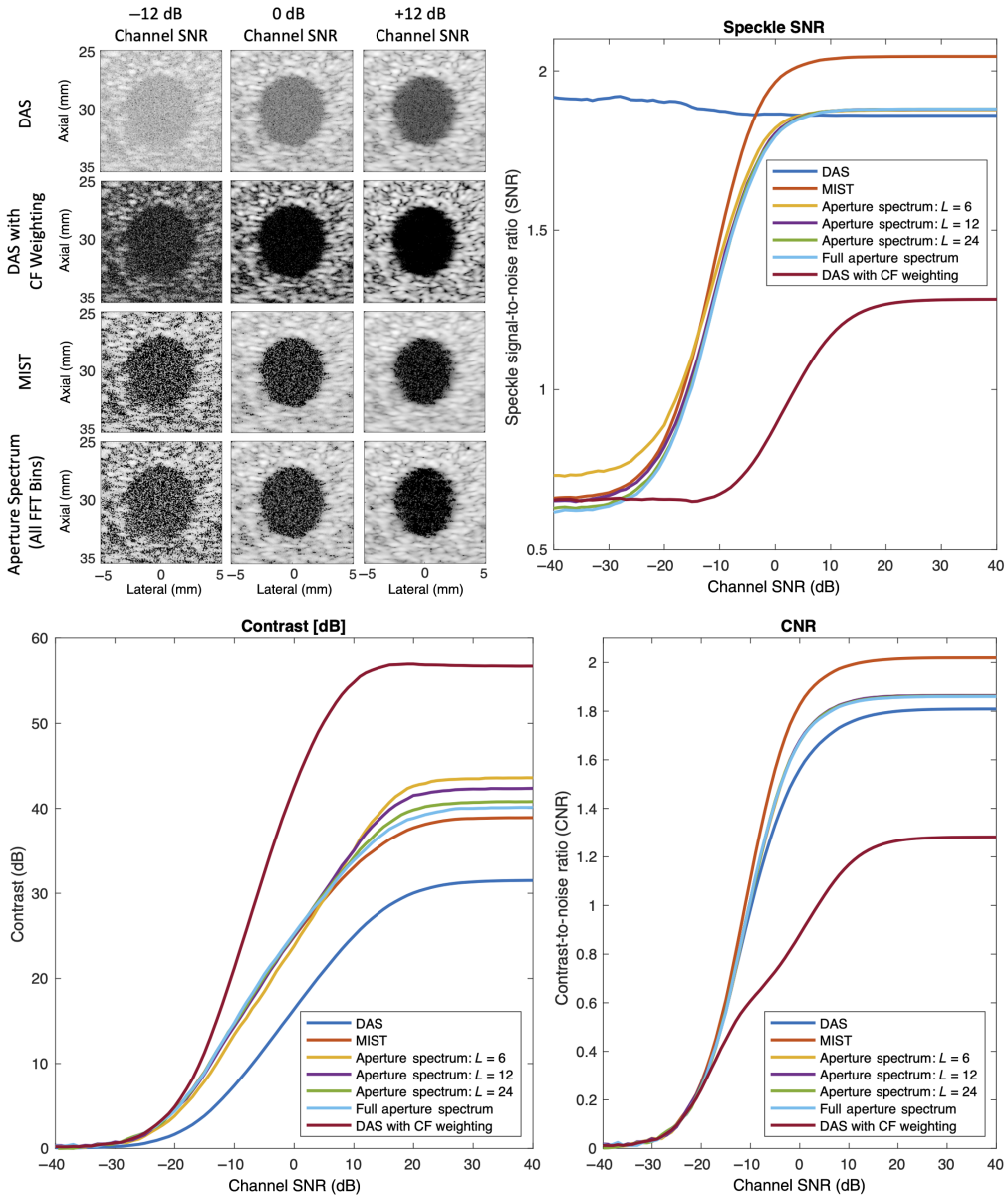

Fig. 6 Measurements of lesion contrast, lesion CNR, and speckle SNR for DAS beamforming, DAS with CF weighting, MIST, and the proposed aperture spectrum methods ($L = 6,12,24$ and the full aperture spectrum) as a function of channel SNR. These measurements were made in the 3.0-mm radius anechoic lesion simulation.

red circle and speckle region outside the outermost red circle in Fig. 5(a). Speckle SNR is computed based on the speckle region outside the outermost red circle. Additionally, Fig. 6 plots lesion contrast, lesion CNR, and speckle SNR as a function of channel SNR in the 3.0-mm anechoic lesion.

MIST and the aperture spectrum approach improve lesion contrast over conventional DAS beamforming at each lesion radius. The aperture spectrum approach achieves higher contrast than MIST at each lesion radius, and the contrast of the aperture spectrum approach increases as the value of L decreases. However, MIST yields the highest speckle SNR, whereas the aperture spectrum approach yields the speckle SNR values closest to conventional DAS. From the B-mode images shown in Fig. 5(a), the aperture spectrum approach appears to preserve the texture of the background speckle seen in DAS, whereas MIST appears to have a blurring effect on the speckle texture. The speckle SNR metric reflects the smoothness of the texture in the background speckle between the imaging techniques. Finally, CNR represents a combination

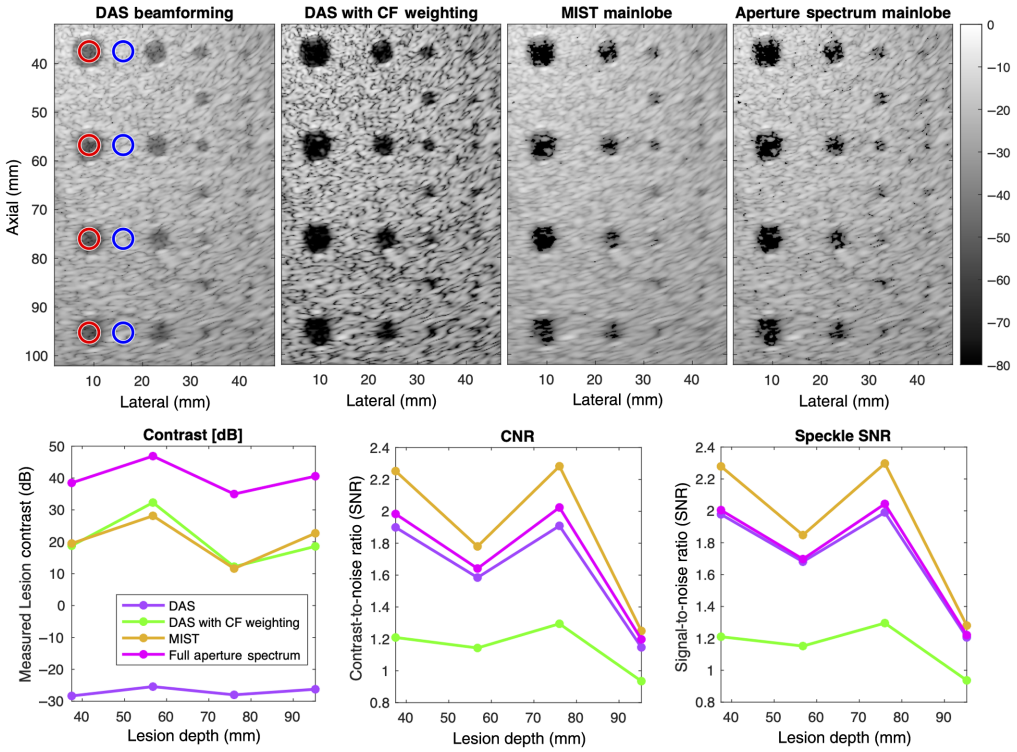

Fig. 7 Comparison of DAS beamforming, MIST, and the proposed aperture spectrum methods for anechoic lesions *in vitro*. These anechoic lesions are found in the ATS Model 539 CIRS phantom. Contrast, CNR, and speckle SNR were computed based on the target and background regions circled in red and blue, respectively.

of contrast and speckle SNR as an imaging metric. MIST has the highest CNR, followed by the aperture spectrum approach and then conventional DAS beamforming. Although CF weighting increases image contrast in DAS, speckle SNR and CNR are much lower as well. These trends in the lesion contrast, lesion CNR, and speckle SNR are also seen *in vitro* (Fig. 7).

4.3 *Preservation of Intrinsic Contrast*

Figures 8 and 9 demonstrate the preservation of intrinsic target contrast in conventional DAS beamforming and the aperture spectrum method. Figure 8 plots the contrast as a function of the channel SNR for simulated hypoechoic and hyperechoic lesions. Figure 9 demonstrates the preservation of intrinsic contrast *in vitro*. In both cases, CF weighting of the DAS image exaggerates the true contrast of the imaging target. This exaggeration is problematic because it does not represent a true improvement in the image quality. A similar improvement in the nominal contrast could be obtained by simply scaling the decibel-scale B-mode image by a factor of 2. However, scaling the image in this way does not retain the true intrinsic contrast of the imaging target nor does it represent a meaningful improvement in image quality. A similar issue occurs when interpreting the contrast improvement resulting from a CF weighting. In fact, the CF weighting lowers the CNR (Fig. 7).

4.4 *In Vivo Imaging Examples*

Figure 10 shows the mainlobe and sidelobe separation in (a) an apical four-chamber view and (b) a parasternal long-axis view of the heart, using the vector scan sequence on the Siemens 5V1 transducer. In each case, the mainlobe MIST and aperture spectrum images improve contrast, which is measured between the regions circled in red for each image. Figure 10(a) specifically highlights the septal wall (circled in yellow) in the mainlobe and sidelobe images in the apical

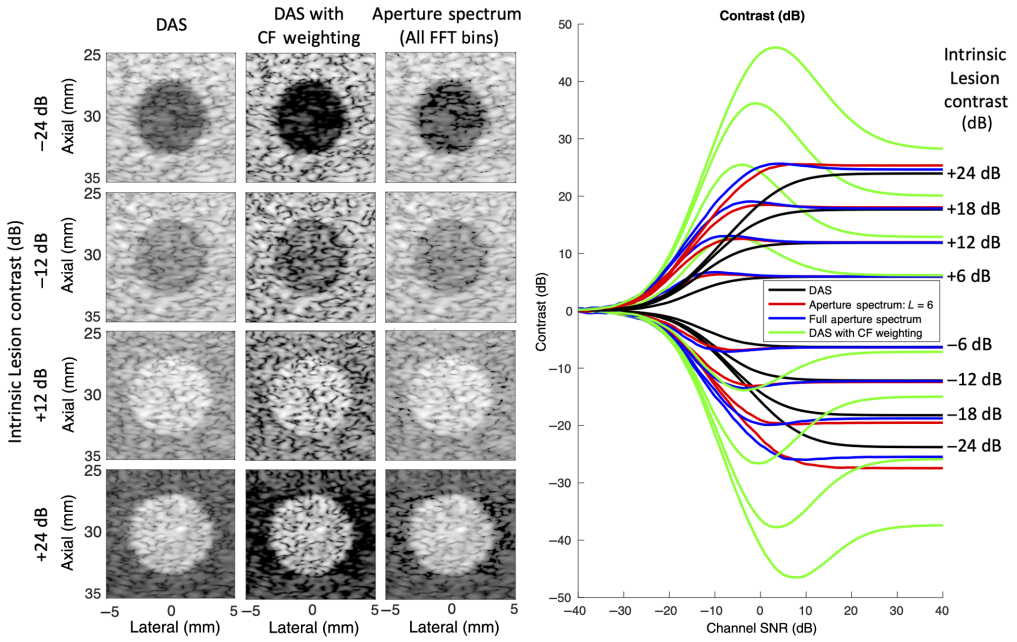

Fig. 8 Preservation of intrinsic target contrast with DAS beamforming, DAS with CF weighting, and the proposed aperture spectrum methods with simulated hypoechoic and hyperechoic lesions as a function of channel SNR. The aperture spectrum approach (for $L = 6$ and the full aperture spectrum) generally preserves the intrinsic contrast of the imaging target. However, CF weighting exaggerates the contrast in the image.

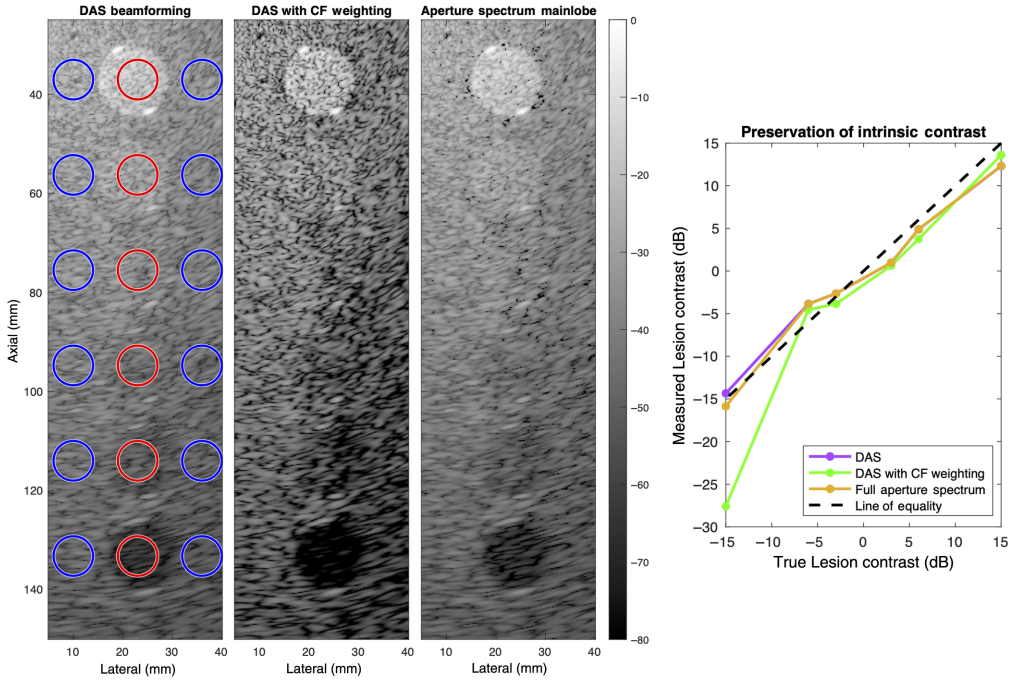

Fig. 9 Preservation of intrinsic target contrast with DAS beamforming, DAS with CF weighting, and the proposed aperture spectrum methods with hypoechoic and hyperechoic lesions in the ATS Model 539 Phantom. Contrast was computed based on the target and background regions circled in red and blue, respectively.

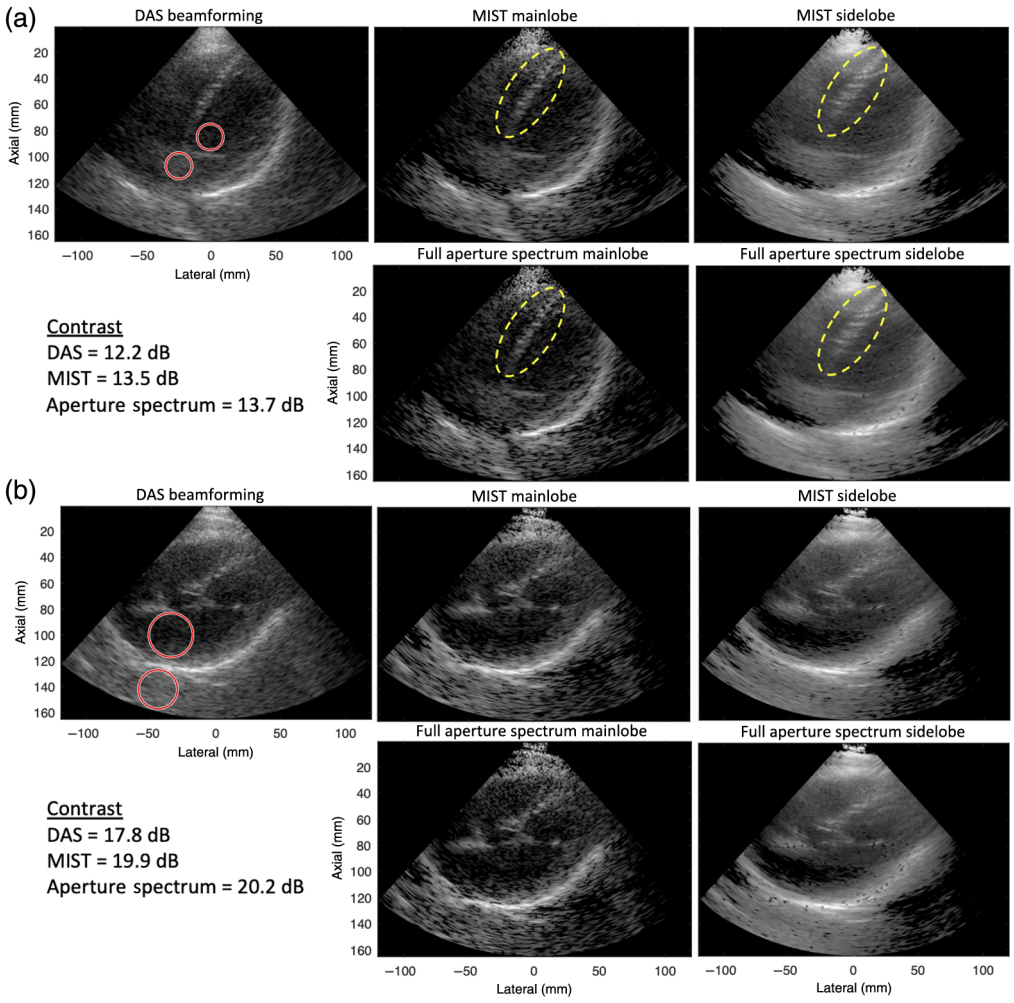

Fig. 10 Separation of mainlobes and sidelobes in cardiac images using MIST and the proposed aperture spectrum approach in phantom experiments. (a) Apical four-chamber view and (b) parasternal long-axis view. Each image is shown at the 60 dB dynamic range. Contrast is computed between the red-circled regions. Yellow-dashed ovals highlight the septum in the mainlobe and sidelobe images.

four-chamber view of the heart. Both techniques show the separation of mainlobe and sidelobes at the septal wall comparable to the point targets seen in Fig. 4.

Figure 11 demonstrates a system-specific implementation of the aperture spectrum approach using standard dynamic-receive focusing and virtual source synthetic aperture. Four different examples are used to assess the impact of virtual source synthetic aperture on the aperture spectrum approach: (1) a grid of anechoic lesions, (2) an edge phantom, (3) an apical four-chamber view of the heart, and (4) a parasternal long-axis view of the heart. In each case, the virtual source synthetic aperture reduces the signal dropout in the near field and improves the reconstructed mainlobe images at all imaging depths. Optimal transmit focusing is generally achieved by multistatic synthetic aperture using each single-element transmit to synthesize a transmit focus at each imaging point. A focused transmit sequence may be designed such that the result of virtual source synthetic aperture best reproduces the focusing achieved by the multistatic setup. This transmit sequence would yield optimal performance from both MIST and the aperture spectrum methods.

Figure 12 shows thyroid and carotid images acquired on two different imaging systems: a commercial L10-4 probe on a Siemens scanner and an L12-3v probe on a Verasonics Vantage 256 research system. Two acquisitions are shown for each imaging system. Each acquisition compares DAS beamforming, DAS with CF weighting, MIST, and the proposed aperture

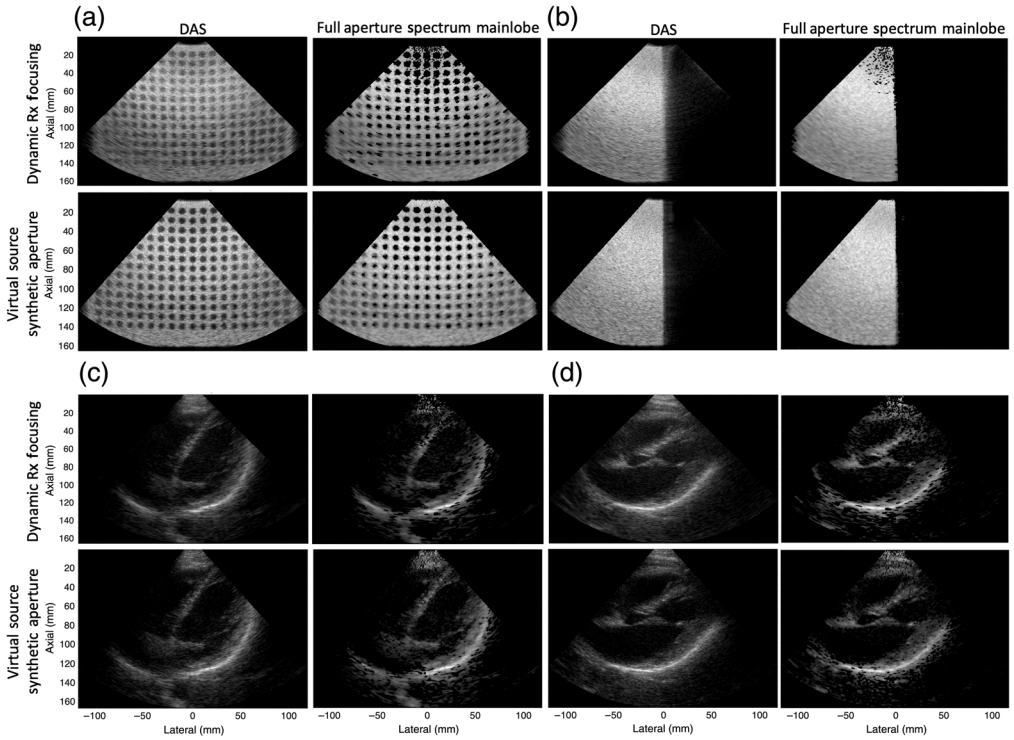

Fig. 11 Impact of virtual source synthetic aperture on the proposed aperture spectrum approach. (a) Field II simulation of anechoic lesions (radii = 4.0 mm), (b) field II simulation of an edge phantom, (c) apical four-chamber view of the heart, and (d) parasternal long-axis view of the heart. Each image is shown at the 50-dB dynamic range. Virtual source synthetic aperture improves the performance of the aperture spectrum approach throughout the image and reduces signal dropout in the near field.

spectrum methods (using the full aperture spectrum). Each image reports the lesion contrast, lesion CNR, and speckle SNR between the anechoic regions circled in red and the speckle background in blue. In each case, both MIST and the aperture spectrum methods improve the contrast of the imaging target while preserving the speckle SNR and lesion CNR found in conventional DAS beamforming. The aperture spectrum method generally appears to yield higher contrast but lower speckle SNR and lesion CNR than MIST. Prior literature[13,24] has also proposed the application of CF weighting to DAS images to improve imaging contrast. However, these results show that the increase in contrast is also accompanied by lower speckle SNR and lesion CNR. Additionally, Figs. 8 and 9 have shown that the CF weighting exaggerates the true contrast of the imaging target.

Figure 13 shows two different abdominal imaging examples that compare the four imaging techniques. The top example shows the gallbladder and inferior vena cava in the field of view. Both MIST and the aperture spectrum methods (using the full aperture spectrum) improve the contrast of the gallbladder while roughly preserving the speckle SNR and lesion CNR found in the DAS image. Once again, although a CF weighting to DAS yields the highest imaging contrast, it also yield a much lower CNR and speckle SNR. In general, CF weighting does not appear to retain the intrinsic contrast of the imaging target and greatly sacrifices speckle SNR and CNR to achieve this exaggerated contrast. The bottom example shows a cross-section view of the kidney at a higher dynamic range (70 dB) to emphasize that MIST and the aperture spectrum methods can be used to identify the anechoic spaces within the kidney much more easily.

5 Discussion

Although both MIST and the proposed aperture spectrum techniques can separate mainlobes and sidelobes in an ultrasound image, the main difference between the two techniques is the domains

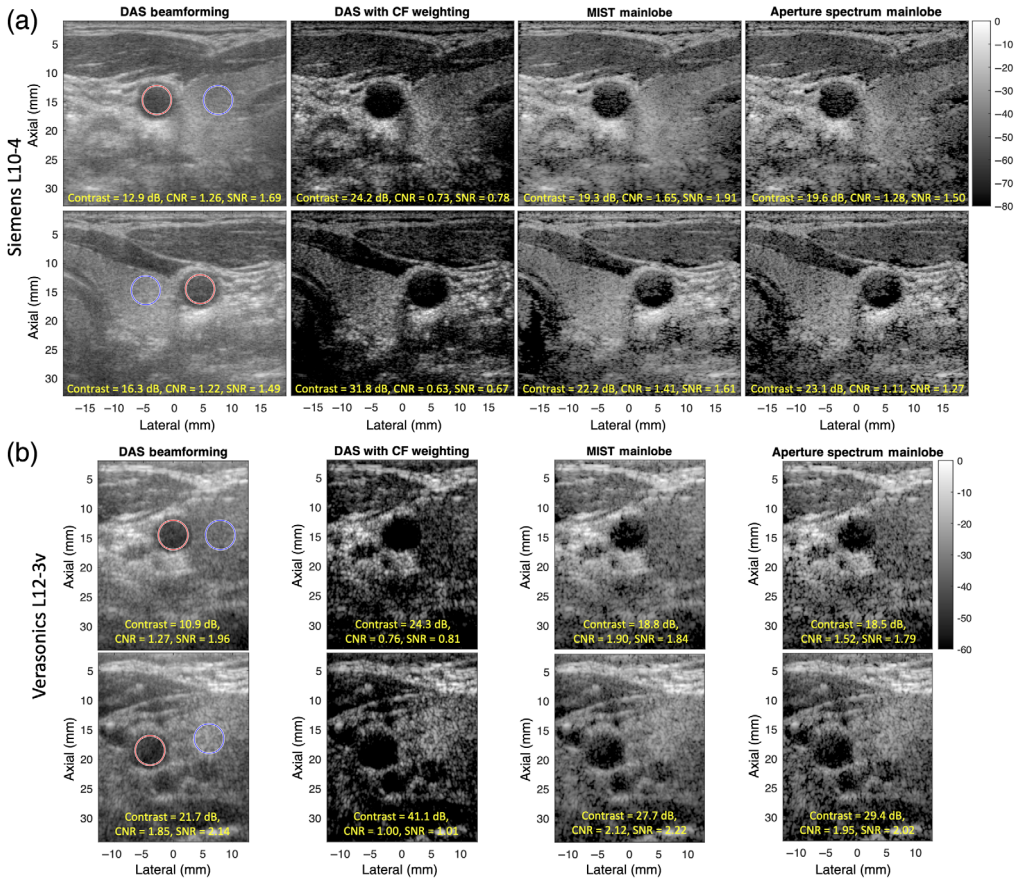

Fig. 12 Comparison of DAS beamforming, DAS with CF weighting, MIST, and the proposed aperture spectrum methods for thyroid and carotid imaging. (a) Using L10-4 probe on Siemens research scanner and (b) using L12-3v probe on a Verasonics Vantage 256 system. Contrast, CNR, and speckle SNR were computed based on the target and background regions circled in red and blue, respectively.

in which they operate. MIST requires the formation of a covariance matrix for received channel data, which requires N^2 multiplications and storage per imaging point, whereas the aperture spectrum technique performs the fast Fourier transform of the received channel data, which requires $O(N \log N)$ operations and N storage per imaging point. As a result, the aperture spectrum method reduces the computational complexity of the mainlobe–sidelobe separation by a factor of $O(N/\log N)$ and the storage requirements by a factor of N. Using a 2.3-GHz 8-Core Intel Core i9 processor, a MATLAB implementation of the aperture spectrum method is roughly 9 times faster than that of MIST. These computation times should roughly scale to the GPU as each imaging technique can be computed in parallel across the pixels in the image. The factor of N difference in the storage requirements can also be significant for a real-time ultrasound imaging system. For example, if $N = 128$, MIST would need 5.9 GB of memory to store all of the covariance matrices needed for a 300×300 pixel ultrasound image, whereas the aperture spectrum method would only need a total of 46 MB to store the aperture spectrum at each imaging point.

The domain in which the separation of mainlobe and sidelobes occurs in the aperture spectrum method also has an impact on its behavior and performance. One interesting difference between the mainlobe–sidelobe decompositions of MIST and the aperture spectrum methods is the axial behavior of the sidelobe images seen in Fig. 3. The sidelobe image of MIST is nulled in a circular region around where the mainlobe would be, whereas the sidelobe images for the aperture spectrum method are nulled in an axially longer but narrower region through the mainlobe area. Another important difference between the mainlobe images of MIST and the aperture spectrum methods is that the aperture spectrum method suppresses the tails of the PSF more

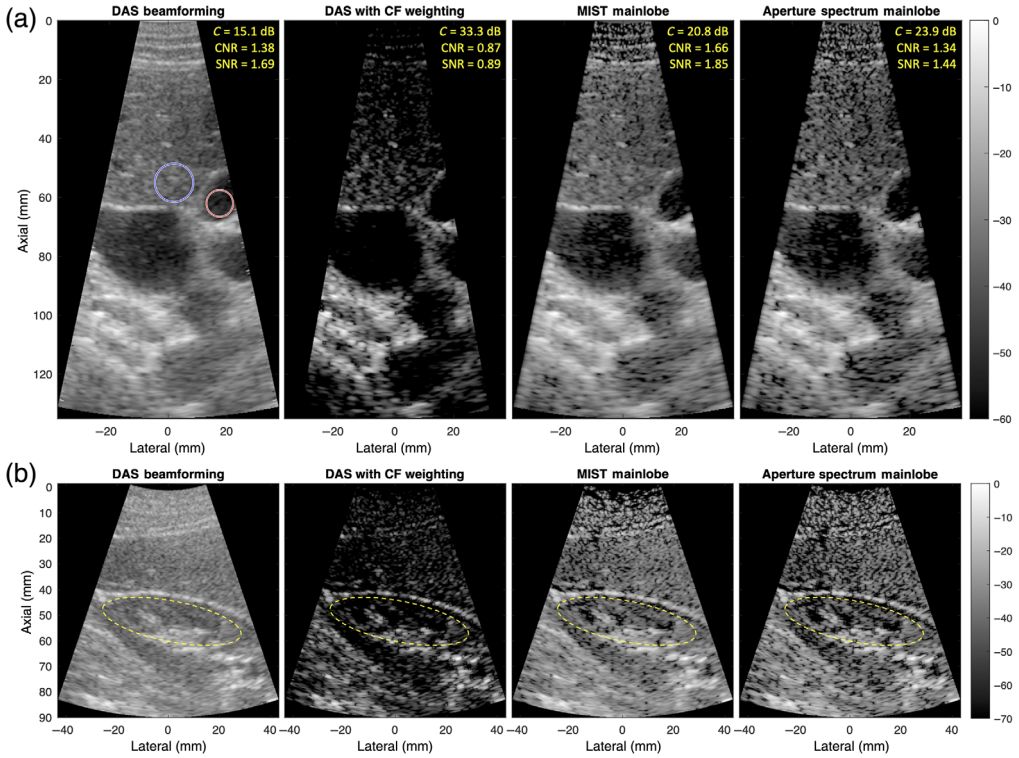

Fig. 13 Comparison of DAS beamforming, DAS with CF weighting, MIST, and the proposed aperture spectrum methods in abdominal imaging. (a) The right-upper quadrant including the liver (blue circle) and gallbladder (red circle) anterior to the inferior vena cava and other abdominal structures. Lesion contrast, lesion CNR, and speckle SNR are calculated based on the regions circled in red and blue. (b) The improved sensitivity of both MIST and the aperture spectrum methods to identify the renal pyramids (anechoic spaces) within the kidney (circled in yellow).

strongly, and decreasing the value of L further suppresses these tails. This increased suppression of the tails of the PSF also explains why the aperture spectrum method exhibits higher contrast than MIST in the anechoic lesions (Fig. 5), especially at lower values of L. However, decreasing L also leads to the misidentification of sidelobe energy as noise. The regions nulled to the left and right in the sidelobe images are attributed to noise during the decomposition process, and these misidentified regions expand as L decreases. Based on the misidentification of sidelobe energy as noise, the improvement in contrast as L decreases may seem counterintuitive. The reason that sidelobe energy becomes misidentified as noise is that most of the information relevant to distinguishing sidelobe energy from noise is contained within the higher frequency components of the aperture spectrum. However, most of the information needed to separate mainlobe energy from sidelobes and noise is contained within the low-frequency bins. So although the separation of sidelobes from noise suffers, the separation of mainlobes from the combination of sidelobes and noise improves as L decreases. However, the exception to this trend occurs at $L = 3$, which is the minimum value of L for which the non-negative least-squares problem in Eq. (7) has a single well-defined solution. In practice, L must be large enough to avoid the misidentification of sidelobe energy as noise but small enough to optimize computation time and imaging contrast. For most of this work, a conservative choice of $L = N/2$ is used to prioritize robustness to noise over gains in contrast and speed.

Another key difference between MIST and the aperture spectrum methods is their behavior in a purely diffuse-scattering background. The speckle SNR produced by MIST is consistently higher than conventional DAS beamforming and the aperture spectrum methods, which also results in MIST having a higher CNR. The elevated speckle SNR and CNR in MIST can be attributed to how MIST appears to have a blurring effect on the background speckle texture as seen in Figs. 5(a), 6, and 7. In these examples, the aperture spectrum method yields speckle SNR and CNR values closer to those of conventional DAS beamforming because the aperture

spectrum method appears to better retain the texture of the underlying speckle. This difference between the MIST and aperture spectrum methods also plays a role *in vivo* (Figs. 10, 12, and 13) with more signal dropout being observed in the image produced by the aperture spectrum method.

An important issue common to both MIST and the aperture spectrum methods is the issue of transmit focusing. The main difference between the field II simulations (Figs. 3 and 5) and the channel data captured on the Siemens 5V1 probe (Figs. 4, 10, and 11) is the transmit sequence that is applied. The field II simulations use multistatic synthetic aperture, whereas the research scanner uses a focused transmit sequence (Table 3). This difference in the acquisition sequence has important implications for both MIST and aperture spectrum methods because the underlying VCZ theorem assumes that the received signals come from a focused source in a diffuse-scattering medium. Although this assumption holds for multistatic synthetic aperture, in which transmit focusing is achieved at all imaging points, this assumption does not hold for a focused transmit beam, in which transmit focusing is only achieved at the focus of the transmit beam.

The implications of fixed transmit focusing are seen in Fig. 4(b), where there is significant signal dropout in the near field for the mainlobe images of both MIST and the aperture spectrum methods. This signal dropout is due to the misidentification of the near-field speckle signal as off-axis scattering due to the sidelobes. This misidentification occurs because the covariance matrices and aperture spectra modeled for mainlobe and sidelobe contributions are no longer accurate far from the transmit focus. Conversely, the sidelobe images in Fig. 4(b) show more signal dropout near the region of the transmit foci because more of the signal in that region is attributed to mainlobes. One way to overcome the depth dependence of MIST and the aperture spectrum methods is to improve transmit focusing at all depths by applying virtual source synthetic aperture. Figure 11 shows that virtual source synthetic aperture removes near-field dropout in the aperture spectrum mainlobe images. This improvement as a result of virtual source synthetic aperture has also been shown in MIST.[19] These transmit focusing effects generally appear to play a larger role in signal dropout than the type of ultrasound probe used (e.g., linear versus curvilinear).

In contrast, the mainlobe-sidelobe separation in point targets does not depend on the location of the point target relative to the transmit focus or the transmit focusing scheme because the backscatter from a strong coherent scatterer is invariant to the transmit sequence applied. In both an anechoic background [Fig. 4(a)] and a diffuse-scattering background [Fig. 4(b)], MIST and the aperture spectrum methods achieve the mainlobe–sidelobe separation for point targets at all imaging depths. A similar mainlobe–sidelobe separation is seen along the septal wall (circled in yellow) in the cardiac images shown in Fig. 10(a). The red circles in Fig. 4(b) highlight strong sidelobes induced at the right and left edges of the phantom because the sudden drop-off in signal intensity at these locations results in off-axis signals measured across the aperture. As observed in Fig. 3, the sidelobe images in Figs. 4 and 10 show nulls where the mainlobe would be located for both MIST and the aperture spectrum methods. Additionally, both methods remain relatively robust to changes in the transmit apodization. Although the mainlobe and sidelobe separation was originally developed using the VCZ theorem for a rectangular transmit apodization, we demonstrated the utility of these approaches on data acquired from a Siemens scanner in which a half-circle apodization was used instead.

Ultimately, ultrasonic backscatter *in vivo* is neither the result of pure diffuse scattering or point reflectors. Backscattering can also originate from specular reflections and spatial fluctuations in backscatter intensity. Specular reflections generally occur at the interface between two different types of tissue because of the mismatch in acoustic impedance (e.g., interfaces between fat, muscle, and connective tissue in the abdominal wall). Specular reflections are distinct from point or diffuse scattering, which result from smaller acoustic impedance changes from subresolution structures inside the same tissue (e.g., diffuse scattering from inside the liver, which appears as speckle in the ultrasound image). Even in the presence of diffuse scattering, the strength of the backscattered signal can vary inside the same tissue. These spatial fluctuations in backscatter may deviate from the pure diffuse scattering model used in the VCZ theorem. The interaction between these multiple sources of ultrasound backscatter may deviate from the underlying pure diffuse scattering model used in the VCZ theorem underlying both MIST and the

aperture spectrum methods. Despite this limitation, MIST and the aperture spectrum methods can image a variety of *in vivo* structures (Figs. 10, 12, and 13) and improve imaging contrast.

However, the main limitation of both imaging techniques is signal dropout. The signal dropout is the result of the underlying non-negative least squares optimization problem in MIST and the aperture spectrum methods because the harsh non-negativity constraint causes the estimate of the mainlobe contribution to go to zero in various parts of the image. Spatial averaging of the receive covariance and aperture spectrum could reduce the effect of signal dropout in these images. Alternatively, the non-negative least-squares optimization problem could be modified to account for signal dropout. Based on all *in vivo* results presented in this work, MIST appears to have less signal dropout than the aperture spectrum method. This trade-off between MIST and the aperture spectrum methods plays an important role in deciding which method is more suitable for a particular application. For a portable low-power system, the angular spectrum approach becomes the obvious choice because of its low computational cost and similar performance to MIST. Modifications to the aperture spectrum method could be used to address signal dropout. On the other hand, the MIST would be more favorable on a larger ultrasound scanner that has the computing capability. MIST remains the more robust approach *in vivo* based on the results presented and exhibits less signal dropout. Future work could also incorporate retrospective encoding for conventional ultrasound sequences[25,26] into MIST and the aperture spectrum methods to overcome effects related to transmit focusing.

6 Conclusions

Previous work on MIST demonstrates that the contribution of mainlobes, sidelobes, and noise to an ultrasound image can be estimated from the covariance of backscattered receive signals. This work demonstrates that a similar decomposition can be performed using the aperture spectrum of the backscattered receive signal, which greatly reduces both computational and storage requirements for real-time imaging applications. The aperture spectrum approach also demonstrates improvements in imaging contrast beyond both conventional DAS B-mode and MIST.

Disclosures

Rehman Ali acquired certain datasets used in this work from a Siemens research scanner during a paid summer internship at Siemens Healthineers. However, there are no financial conflicts of interest to disclose pertaining to this work.

Acknowledgments

Rehman Ali was funded by the National Defense Science and Engineering Graduate fellowship during his time as a graduate student at Stanford University. This work was also partially funded by the National Institute of Biomedical Imaging and Bioengineering (Grant Nos. R01-EB027100 and R01-EB013661). The authors would also like to thank Rick Loftman, Ismayil M. Guracar, and Vasant Salgaonkar at Siemens Healthineers for enabling *in vivo* demonstration of this work using channel data captured on the Siemens research scanner.

Code, Data, and Materials Availability

To make our efforts more accessible to the broader research community, we have provided sample code and channel data for a 3.5-mm radius anechoic lesion at https://github.com/rehmanali1994/MainlobeSidelobeSeparation (DOI: 10.5281/zenodo.5880090)

References

1. D. Liu et al., "Coherence factor adaptive ultrasound imaging," US Patent App. 11/046,347 (2006).

2. K. Hollman, K. Rigby, and M. O'donnell, "Coherence factor of speckle from a multi-row probe," in *IEEE Ultrason. Symp. Proc. Int. Symp.*, IEEE, Vol. 2, pp. 1257–1260 (1999).
3. R. Mallart and M. Fink, "Adaptive focusing in scattering media through sound-speed inhomogeneities: the van Cittert–Zernike approach and focusing criterion," *J. Acoust. Soc. Am.* **96**(6), 3721–3732 (1994).
4. P.-C. Li and M.-L. Li, "Adaptive imaging using the generalized coherence factor," *IEEE Trans. Ultrason. Ferroelectr. Freq. Control* **50**(2), 128–141 (2003).
5. J. Camacho, M. Parrilla, and C. Fritsch, "Phase coherence imaging," *IEEE Trans. Ultrason. Ferroelectr. Freq. Control* **56**(5), 958–974 (2009).
6. M. A. Lediju et al., "Short-lag spatial coherence of backscattered echoes: imaging characteristics," *IEEE Trans. Ultrason. Ferroelectr. Freq. Control* **58**(7), 1377–1388 (2011).
7. D. Hyun, A. L. C. Crowley, and J. J. Dahl, "Efficient strategies for estimating the spatial coherence of backscatter," *IEEE Trans. Ultrason. Ferroelectr. Freq. Control* **64**(3), 500–513 (2017).
8. R. Mallart and M. Fink, "The van Cittert–Zernike theorem in pulse echo measurements," *J. Acoust. Soc. Am.* **90**(5), 2718–2727 (1991).
9. J. Shin and L. Huang, "Spatial prediction filtering of acoustic clutter and random noise in medical ultrasound imaging," *IEEE Trans. Med. Imaging* **36**(2), 396–406 (2017).
10. J. Shin, L. Huang, and J. T. Yen, "Spatial prediction filtering for medical ultrasound in aberration and random noise," *IEEE Trans. Ultrason. Ferroelectr. Freq. Control* **65**(10), 1845–1856 (2018).
11. I. K. Holfort, F. Gran, and J. A. Jensen, "Broadband minimum variance beamforming for ultrasound imaging," *IEEE Trans. Ultrason. Ferroelectr. Freq. Control* **56**(2), 314–325 (2009).
12. B. M. Asl and A. Mahloojifar, "Eigenspace-based minimum variance beamforming applied to medical ultrasound imaging," *IEEE Trans. Ultrason. Ferroelectr. Freq. Control* **57**(11), 2381–2390 (2010).
13. C.-I. C. Nilsen and S. Holm, "Wiener beamforming and the coherence factor in ultrasound imaging," *IEEE Trans. Ultrason. Ferroelectr. Freq. Control* **57**(6), 1329–1346 (2010).
14. J. Zhao et al., "Coherence factor and wiener postfilter in synthetic aperture ultrasound imaging," *J. Acoust. Soc. Am.* **141**(3), 2177–2190 (2017).
15. B. Byram et al., "A model and regularization scheme for ultrasonic beamforming clutter reduction," *IEEE Trans. Ultrason. Ferroelectr. Freq. Control* **62**(11), 1913–1927 (2015).
16. K. Dei, S. Schlunk, and B. Byram, "Computationally efficient implementation of aperture domain model image reconstruction," *IEEE Trans. Ultrason. Ferroelectr. Freq. Control* **66**(10), 1546–1559 (2019).
17. M. R. Morgan, G. E. Trahey, and W. F. Walker, "Multi-covariate imaging of sub-resolution targets," *IEEE Trans. Med. Imaging* **38**(7), 1690–1700 (2019).
18. M. R. Morgan, G. E. Trahey, and W. F. Walker, "Intrinsic tradeoffs in multi-covariate imaging of sub-resolution targets," *IEEE Trans. Ultrason. Ferroelectr. Freq. Control* **67**(10), 1980–1992 (2020).
19. M. R. Morgan et al., "Synthetic aperture focusing for multi-covariate imaging of sub-resolution targets," *IEEE Trans. Ultrason. Ferroelectr. Freq. Control* **67**(6), 1166–1177 (2020).
20. S. D. Silverstein, "Ultrasound scattering model: 2-D cross-correlation and focusing criteria-theory, simulations, and experiments," *IEEE Trans. Ultrason. Ferroelectr. Freq. Control* **48**(4), 1023–1030 (2001).
21. R. Ali, "Separation of mainlobe and sidelobe contributions to b-mode ultrasound images based on the aperture spectrum," *Proc. SPIE* **12038**, 1203806 (2022).
22. J. A. Jensen, "Field: a program for simulating ultrasound systems," in *10th Nordicbaltic Conf. Biomed. Imaging*, Citeseer, Vol. 4, supplement 1, part 1, pp. 351–353 (1996).
23. J. A. Jensen and N. B. Svendsen, "Calculation of pressure fields from arbitrarily shaped, apodized, and excited ultrasound transducers," *IEEE Trans. Ultrason. Ferroelectr. Freq. Control* **39**(2), 262–267 (1992).

24. B. M. Asl and A. Mahloojifar, "Minimum variance beamforming combined with adaptive coherence weighting applied to medical ultrasound imaging," *IEEE Trans. Ultrason. Ferroelectr. Freq. Control* **56**(9), 1923–1931 (2009).
25. N. Bottenus, "Recovery of the complete data set from focused transmit beams," *IEEE Trans. Ultrason. Ferroelectr. Freq. Control* **65**(1), 30–38 (2018).
26. R. Ali et al., "Extending retrospective encoding for robust recovery of the multistatic dataset," *IEEE Trans. Ultrason. Ferroelectr. Freq. Control* **67**(5), 943–956 (2020).

Rehman Ali received his BS degree in biomedical engineering in 2016 from Georgia Institute of Technology, Atlanta, Georgia, USA, his MS degree in computational and mathematical engineering in 2020, and his PhD in electrical engineering in 2022 from Stanford University, Palo Alto, California, USA. His research interests include signal processing, inverse problems, computational modeling of acoustics, and real-time beamforming algorithms. He is currently at the University of Rochester with Dr. Nebojsa Duric to develop waveform inversion techniques for ultrasound computed tomography.

Trevor Mitcham received his BS degree in bioengineering from Rice University, Houston, Texas, USA, in 2012 and his PhD in medical physics from the University of Texas, MD Anderson Cancer Center, UT Health Graduate School of Biomedical Sciences, Houston, Texas, USA, in 2021. His research interests include ultrasound-mediated molecular imaging, photoacoustic imaging, and ultrasound phantom development. He is currently at the University of Rochester with Dr. Nebojsa Duric to develop a research system for ultrasound computed tomography.

Leandra Brickson received his BS degree in electrical engineering from the University of Minnesota in 2012, his MS degree in electrical engineering from the North Carolina State University in 2015, and his PhD in electrical engineering from Stanford University in 2022. His background includes optics, light transport, and fabrication, with research focused on image processing and deep learning of ultrasound images and volumes under the supervision of Dr. Jeremy Dahl.

Wentao Hu received his BS degree in electrical and computer engineering from the University of Rochester, Rochester, New York, USA, in 2018. His research interests include functional ultrasound imaging, microvessel doppler imaging, and ultrasound beamforming algorithms. He is currently a PhD candidate at the University of Rochester in the Laboratory of Dr. Marvin Doyley, focusing on applying functional ultrasound imaging to study the functionality and organization of the visual cortex with a ferret model.

Marvin Doyley received his PhD in biophysics from the University of London, London, UK, in 2000. In 2008, he joined the Department of Electrical and Computer Engineering at the University of Rochester, Rochester, NY, USA, where is he currently a department chair and a professor (with joint appointments in biomedical engineering and imaging sciences). His research interests include vascular elastography, elastographic imaging, harmonic imaging, and surrogate biomarkers for guiding pancreatic cancer treatment.

Deborah Rubens received her bachelor's degree in biology from Stanford University and her MD from the University of Rochester. She is a professor and associate chair of imaging sciences at the University of Rochester Medical Center. Her primary clinical specialties are ultrasound, body computed tomography, and magnetic resonance imaging. Her research and academic interests include prostate cancer/sonoelasticity, prostate cancer/diagnostic efficacy, contrast agent development-liver and vascular ultrasound, three-dimensional ultrasound, and US/MR/CT fusion.

Zeljko Ignjatovic received his BS degree in electrical engineering from the University of Novi Sad, and his MS degrees and PhD in electrical engineering from the University of Rochester, in 1999, 2001, and 2004, respectively. He is an associate professor of electrical and computer engineering at the University of Rochester. His interests include analog and mixed-signal circuit

design, A/D converters, image sensor architectures, THz imaging arrays, radar and ultrasound imaging techniques, and related signal processing methods.

Nebojsa Duric received his PhD in astrophysics from the University of Toronto. After a 20-year astrophysics career in radio astronomy, he began his new career in medical imaging, first at the Karmanos Cancer Institute and now at the University of Rochester where he serves as a professor and vice chair for research in the Imaging Sciences Department. His research interests are in the field of ultrasound tomography with clinical applications to breast imaging.

Jeremy Dahl received his BS degree in electrical engineering from the University of Cincinnati, Cincinnati, Ohio, USA, in 1999 and his PhD in biomedical engineering from Duke University, Durham, North Carolina, USA, in 2004. He is currently an associate professor in the Department of Radiology at Stanford University, Stanford, California, USA. His current research interests include beamforming, coherence and noise in ultrasonic imaging, and speed of sound estimation.